PERGAMON

International Journal of Heat and Mass Transfer 45 (2002) 585–595

International Journal of HEAT and MASS TRANSFER

www.elsevier.com/locate/ijhmt

Flow characteristics on a heated rotating disc under natural convection dominant conditions

Fumimaru Ogino *, Takaji Inamuro, Kei Mizuta, Atsushi Kino, Ryuji Tomita

Department of Chemical Engineering, Kyoto University, Yoshida, Sakyo-ku, Kyoto 606-8501, Japan

Received 9 February 2001; received in revised form 25 April 2001

Abstract

Characteristics of circumferential vortices, which emerge on a heated rotating disc under natural convection dominant conditions, have been studied experimentally. The techniques of laser induced fluorescence (LIF) and particle image velocimetry (PIV) have been utilized as a non-invasive method to obtain two-dimensional temperature and velocity distributions, respectively. The results show that the frequency of appearance of the vortex increases with increasing buoyancy effect. The ensemble averages of the temperature and vertical velocity as well as those of RMS values of temperature and vertical velocity fluctuations are large in the vortex. Most of heat is transferred vertically by fluctuations in the vortex.

1. Introduction

The boundary layer induced by a rotating disc is of great scientific importance owing to its relevance to applications in turbomachinery and chemical apparatuses such as rotating disc-type chemical vapor deposition reactor.

The disc boundary layer is unique in that it is three-dimensional from its inception. The laminar flow is one of the few non-trivial three-dimensional cases whose exact Navier–Stokes solutions exist [1]. The transitional flow over a rotating disc has been considered by Malik et al. [2], Balachandar et al. [3], Lingwood [4] and others. The experimental investigation of the statistical and structural features of the turbulent boundary layer over a rotating disc has been also conducted by Littell and Eaton [5]. On the other hand, Wu and Squires [6] have used the large eddy simulation to compare their result to the experimental measurements of Littel and Eaton [5].

Several studies of the heat transfer from an isothermal surface have been made by Cobb and Saunders [7], McComas and Hartnett [8], and Popiel and Boguslawski [9]. Elkins and Eaton [10] measured heat transfer from a uniform heat flux surface while Tadros and Erian [11] computed the heat transfer for both isothermal and uniform heat flux conditions.

Compared to those flow characteristics and the forced convection heat transfer in the three-dimensional boundary layer over a rotating disc, the effect of buoyancy has been the subject of considerably fewer investigations. Recently, Ogino et al. [12–14] have showed that circumferential vortices appear on a heated rotating disc under the high uniform heat flux condition and they travel on the disc from the center region to the edge. These vortices are considered to appear by buoyancy effect, because Reynolds number at which they are observed is much smaller than that at which turbulence appears in the isothermal system.

The structure of the circumferential vortices was discussed by Ogino et al. [14]. The circumferential vortices are developed from thermal plumes appearing near the heated rotating disc and have a rotational motion of nearly same scale as the thickness of the velocity boundary layer on the rotating disc.

In this study, the temperature and velocity distributions near the heated rotating disc were measured simultaneously in the r–z plane using laser induced fluorescence (LIF) and particle image velocimetry (PIV), respectively, and then we investigated the effect of these circumferential vortices on the characteristics of the thermal flow field.

* Corresponding author. Tel.: +81-75-753-5561; fax: +81-75-761-3779.

E-mail address: ogino@cheme.kyoto-u.ac.jp (F. Ogino).

0017-9310/02/$ - see front matter
PII: S0017-9310(01)00171-5

Nomenclature

C_p	constant pressure specific heat
g	gravitational acceleration
Gr_q	Grashof number based on wall heat flux ($= \beta g q_w R_d^4/kv^2$)
Gr_{qc}	critical Grashof number ($= 4.01 \times 10^{10}$)
Gr_q^*	normalized Grashof number ($= Gr_q/Gr_{qc}$)
k	thermal conductivity
N_c	number of the detected vortices
N_τ	number of vortices appearing with time interval τ
Pr	Prandtl number ($= \nu/\alpha$)
q_w	heat flux at the wall
$\overline{q_z}^{(d)}$	heat flux by fluctuation
$\overline{q_z^*}^{(d)}$	dimensionless heat flux by fluctuation ($= \overline{q_z}^{(d)}/q_w$)
R_d	disc radius
Re	Reynolds number ($= R_d^2\omega/\nu$)
Re_s	approaching Reynolds number ($= R_d v_{zs}/\nu$)
r	radial distance in cylindrical coordinates
r^*	dimensionless radial distance ($= r/R_d$)
T	temperature
t	time
T_w	wall temperature
T_s	temperature at the inlet of the apparatus
v_r	radial velocity
v_r^*	dimensionless radial velocity ($= v_r/r\omega$)
v_z	vertical velocity
v_z^*	dimensionless vertical velocity ($= v_z/\sqrt{\nu\omega}$)
z	vertical distance in cylindrical coordinates

Greek symbols

β	coefficient of thermal expansion
ζ	dimensionless vertical distance ($= z/\sqrt{\nu/\omega}$)
ν	kinematic viscosity
ρ	density
σ	standard deviation of the error of the temperature measurement by LIF technique
τ	time interval of vortex emerging
ω	angular velocity of rotating disc

Superscripts

$'$	fluctuation
-	average

Subscript

c	conditionally sampled

2. Experimental apparatus and procedures

2.1. Experimental apparatus

Fig. 1 shows the outline of the experimental apparatus. The apparatus consists of an acrylic cylinder of 580 mm in inner diameter and of a rotating disc of 400 mm in diameter and 50 mm in thickness.

A copper disc of 360 mm in diameter and 10 mm in thickness is embedded in the rotating disc, flush with the surface of the rotating disc. The copper disc is heated by an electric heater of 360 mm in diameter and 250 μm thick which is set at the back of the disc. The surface of the copper disc was used as the heat transfer surface. A test calculation shows that a heat loss is less than 1% of total heat produced. Heat flux at the wall, q_w, was

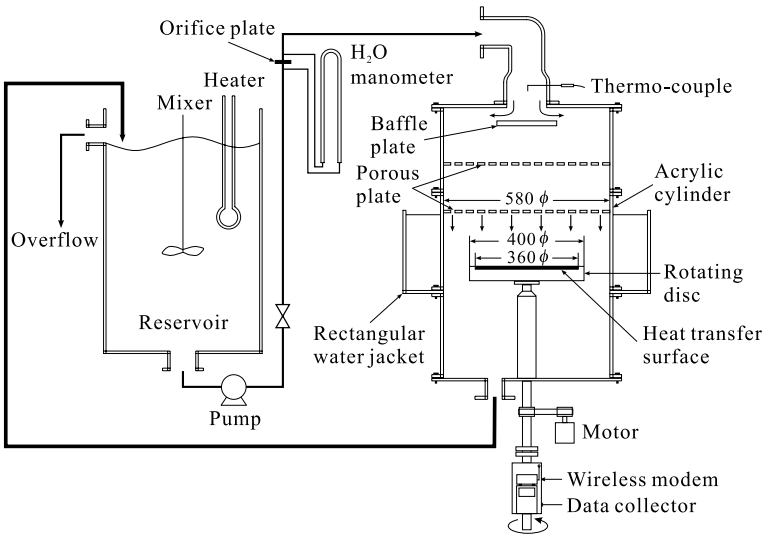

Fig. 1. Schematic diagram of experimental apparatus.

determined from the electric power supplied to the heater which is measured by a digital powermeter.

Fluid used was aqueous solution of Rhodamine B and led from a reservoir tank to the top of the apparatus. The velocity of the flow was made uniform by a baffle plate and two porous plates, and the fluid impinges vertically on the rotating disc.

Wall temperature T_w was measured by 16 CA thermocouples embedded in the copper disc. Bulk temperature of fluid was measured by a sheathed thermocouple at the inlet of the apparatus. Analogue signals from the thermocouples are converted to digital ones, stored to a memory, and then transmitted to a personal computer by way of a RS-232C radio modem.

The rotating speed and inlet flow rate in the steady state were measured with a digital tachometer or a stop watch (at low rotating speed), and an orifice manometer, respectively.

The Reynolds number was set constant as 3.0×10^4. The Reynolds number of approaching flow, Re_s, was 2.0×10^3, the Prandtl number Pr varied from 5.4 to 5.8, and the Grashof number based on the wall heat flux was varied from 7.2×10^{10} to 1.6×10^{11}. The values of Re and Re_s satisfy the criterion that the effect of the approaching flow on the heat transfer at the rotating disc can be neglected [12]. In addition, the value of Re_s is larger than the theoretical value of laminar boundary layer over the rotating disc, $Re_{sc} = 154$, to eliminate a large circulating fluid motion between the porous plate and the rotating disc [15]. The experiment with heated rotating disc was conducted at larger values of the Grashof number than the critical Grashof number, that is, under the natural convection dominant conditions.

2.2. Coordinates and configurations

The coordinates used are shown in Fig. 2. The center of the disc is set as the origin, the radial direction as r axis and the vertical direction as z axis, respectively.

The center of the visualization area of 26.8 mm wide and 10.1 mm high was set at dimensionless radius $r^* = 0.6$, as shown in Fig. 2. We set 61×52 grid within the visualization area for both temperature and velocity measurements, and the distances between each measuring points are 1.49×10^{-1} mm in the radial direction and 1.61×10^{-1} mm in the vertical direction. The distance between the surface of the disc and the lowest grid was 7.26×10^{-1} mm.

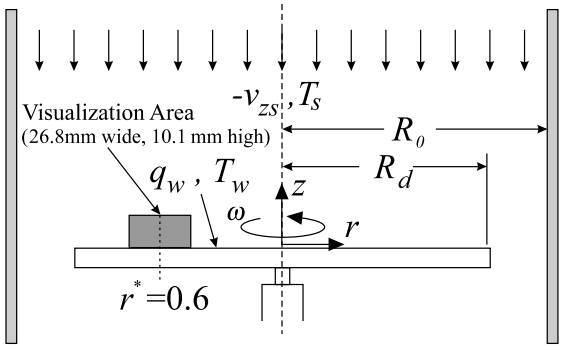

Fig. 2. Coordinate system.

2.3. Image acquisition system

We used an Ar-ion laser (Model 909, American Laser) to illuminate the visualization area. The laser beam was expanded to a sheet shape by a cylindrical lens, and was inserted into the apparatus in the way to involve the axis of the rotating disc.

A digital video camera (DCR-VX1000, Sony) was used for the image acquisition. 4096 successive images were recorded at a run at the intervals of 1/30 s. Recorded images were once stored to a digital video tape, and were transmitted to a personal computer via a digital video capture board (DV-Raptor, Canopus).

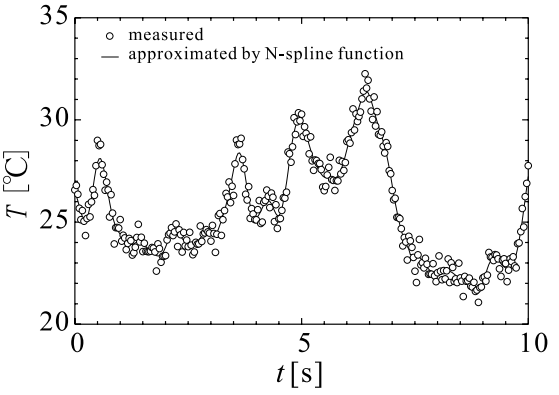

Fig. 3. Example of temperature variation with time.

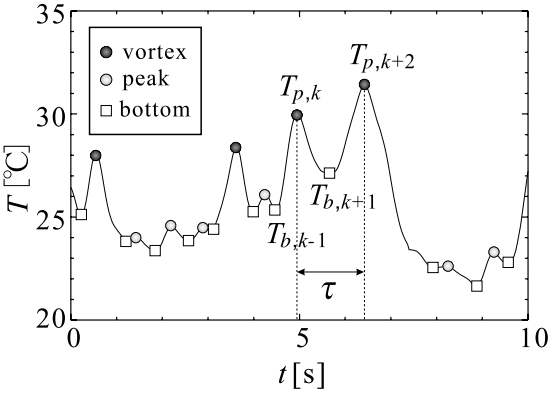

Fig. 4. Detection of temperature signals of vortex.

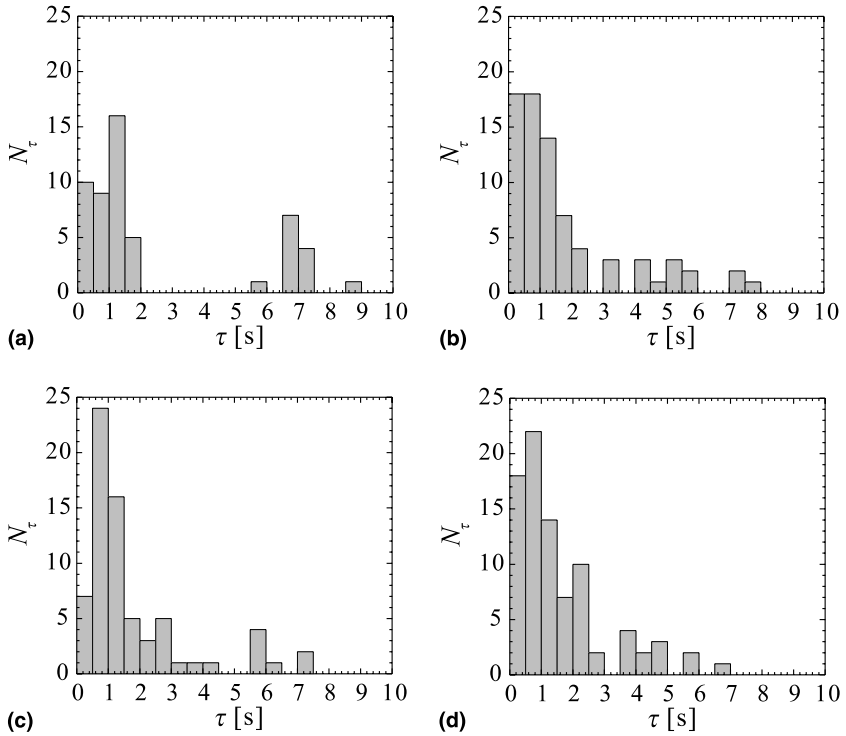

Fig. 5. Frequency distributions of the time interval between the successive appearances of the vortex. (a) $Gr_q^* = 1.79$, (b) $Gr_q^* = 2.76$, (c) $Gr_q^* = 3.13$, (d) $Gr_q^* = 3.98$.

These images were used both in temperature and velocity measurements through successive image processing.

2.4. Temperature measurement

The temperature of the fluid was measured by the fluorescence intensity of the Rhodamine B. The details of the measurement technique are presented by Sakakibara et al. [16]. The concentration of Rhodamine B was 6.5×10^{-5} kg-Rhodamine B/kg-water. Fluorescence intensity was averaged within 7×7 pixels area to reduce noise effect caused by particle reflection. From calibration experiments, it is found that LIF's result is in good agreement with thermocouple's one regardless of the position of the measuring point. Since the average value and the standard deviation of the error of LIF method based on the thermocouple measurement, $(T_{\mathrm{LIF}} - T_{\mathrm{TC}})$, were -8.50×10^{-2} and 0.383 K, respectively, we concluded that this method had enough precision for this experiment.

2.5. Velocity measurement

PIV was used to obtain the velocity distribution of a flow field. This method is widely used for velocity measurement, for example, by Willert and Gharib [17], Hassan et al. [18], and Wozniak and Wozniak [19]. The algorithm used in this study is the cross-correlation technique in which two images are used. One image is recorded at t, and the other is recorded at $t + \Delta t$. First, small area, which is called the reference matrix, is set at t, then the corresponding matrix is

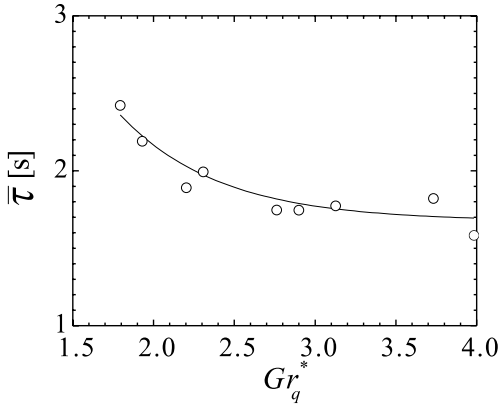

Fig. 6. Variation of the average time interval between the successive appearances of the vortex.

searched over interrogation window set at $t + \Delta t$. Then the displacement, $(\Delta r, \Delta z)$, between the reference matrix and the corresponding matrix is determined from the peak of the cross-correlation coefficient and the velocity components are obtained from the following equations:

$$v_r = \Delta r/\Delta t, \quad v_z = \Delta z/\Delta t. \tag{1}$$

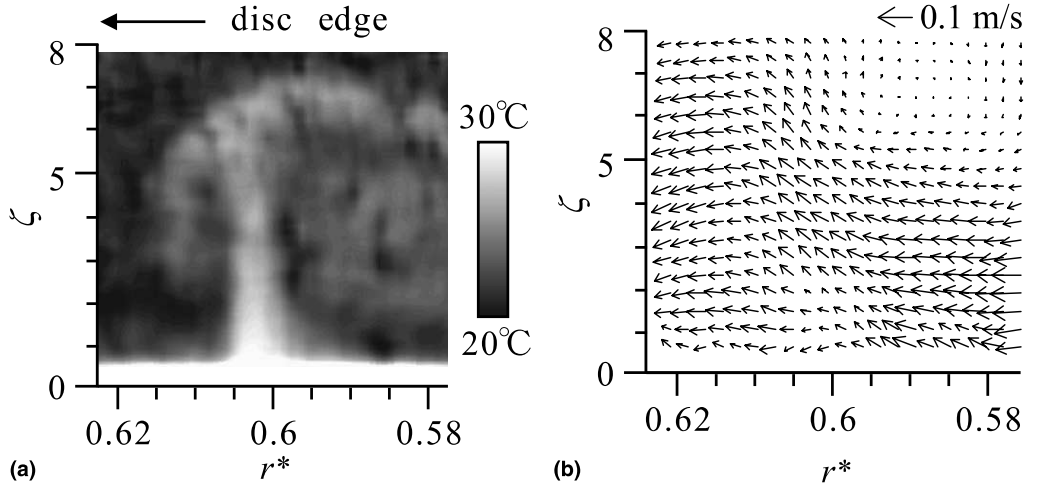

Fig. 7. Example of the measured temperature and velocity distributions. (a) Temperature distribution. (b) Velocity vectors.

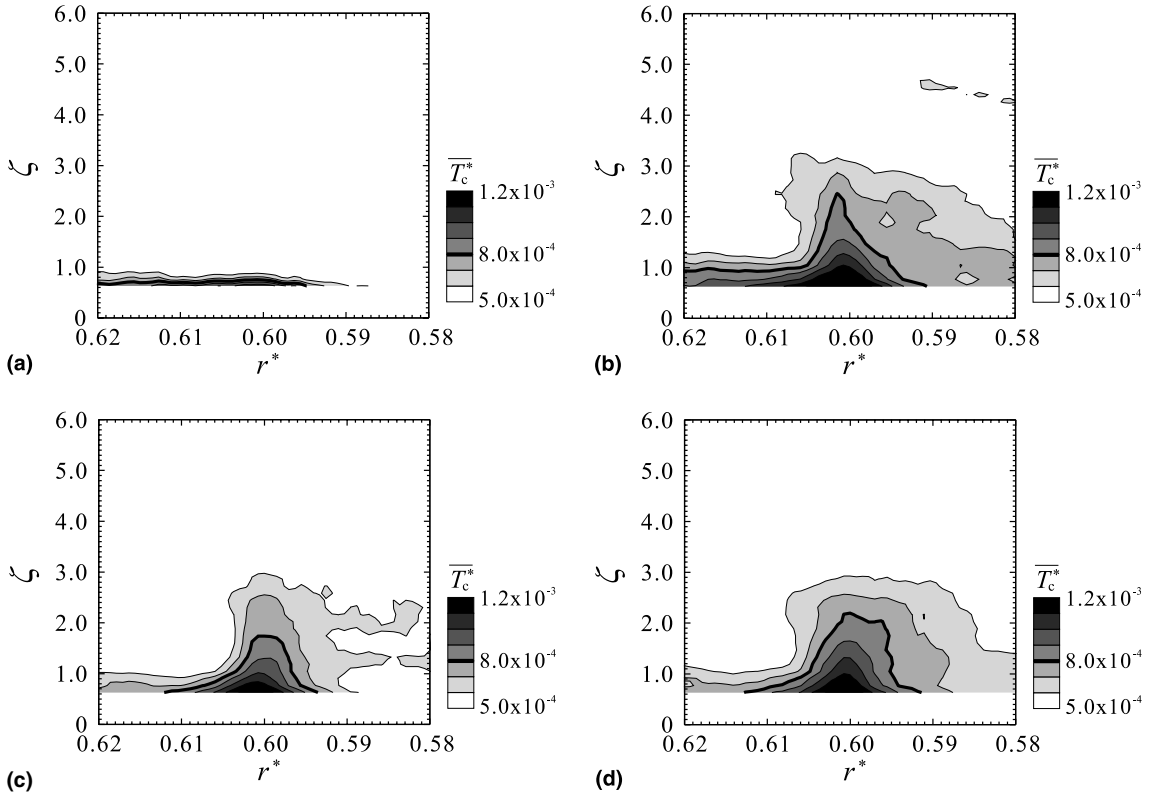

Fig. 8. Distributions of the conditionally averaged temperature. (a) $Gr_q^* = 1.79$, (b) $Gr_q^* = 2.76$, (c) $Gr_q^* = 3.13$, (d) $Gr_q^* = 3.98$.

3. Results and discussion

3.1. Detection of the vortex

Fig. 3 shows an example of the variation of the measured temperature at $r^* = 0.6$ and $z = 7.26\times 10^{-1}$ mm ($\zeta = 0.63$) with time. The solid curve represents a smoothed one by making use of an N-spline function. We fixed all weight coefficients as 1, and varied smoothing parameter in the spline function. We obtained the optimum smoothing function which satisfied the following condition:

$$\left|\sigma - \sqrt{\frac{1}{N}\sum_{i=0}^{N-1}\{T_{i_{\mathrm{cal}}} - T_i\}^2}\right| \Big/ \sigma \leqslant 0.001, \tag{2}$$

where N is the number of original sampling data points, T_i the measured temperature values, $T_{i_{\mathrm{cal}}}$ the calculated temperature values and σ standard deviation of the error of the temperature measurement by LIF technique.

From the temperature variation, we picked up peak and bottom temperatures, $T_{\mathrm{p},k}$ and $T_{\mathrm{b},k+1}$, by the following criteria.

For $i = 1, 2, 3, \cdots, N-1$,

if $T_{(i-1)_{\mathrm{cal}}} < T_{i_{\mathrm{cal}}}$ and $T_{i_{\mathrm{cal}}} > T_{(i+1)_{\mathrm{cal}}}$,

then $T_{\mathrm{p},k} = T_{i_{\mathrm{cal}}}$, (3)

if $T_{(i-1)_{\mathrm{cal}}} > T_{i_{\mathrm{cal}}}$ and $T_{i_{\mathrm{cal}}} < T_{(i+1)_{\mathrm{cal}}}$,

then $T_{\mathrm{b},k+1} = T_{i_{\mathrm{cal}}}$, (3a)

where $k = 1, 2, \ldots$

A result is shown in Fig. 4.

We regarded a signal as the vortex, if the following conditions were satisfied:

$$T_{\mathrm{p},k} > \overline{T} + \sqrt{\overline{T'^2}} \tag{4}$$

and

$$\frac{(T_{\mathrm{p},k} - T_{\mathrm{b},k-1}) + (T_{\mathrm{p},k} - T_{\mathrm{b},k+1})}{2} > 3\sigma, \tag{4a}$$

where $\overline{T}$ is the time averaged temperature, and T' the instantaneous temperature fluctuation. The detected vortices by Eqs. (4) and (4a) corresponded exactly to the vortices determined by eyes from the video image.

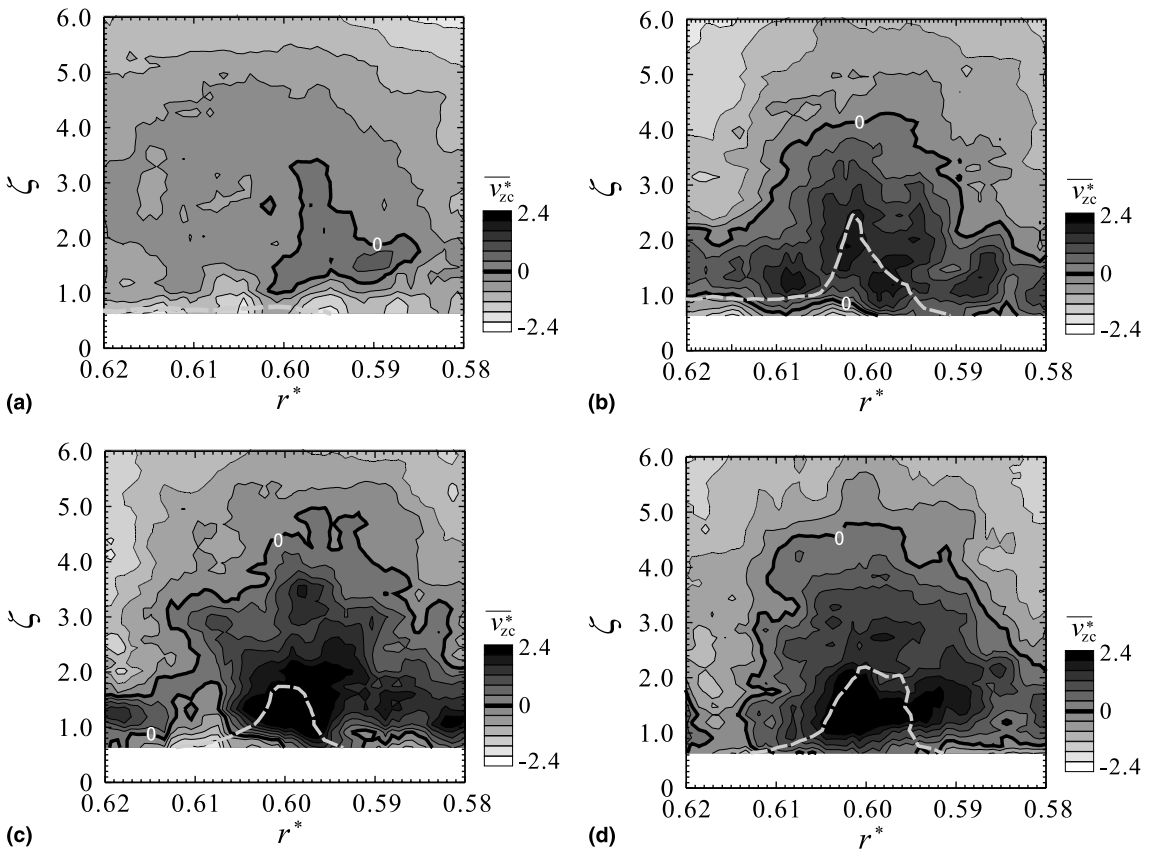

Fig. 9. Distributions of the conditionally averaged vertical velocity. (a) $Gr_q^* = 1.79$, (b) $Gr_q^* = 2.76$, (c) $Gr_q^* = 3.13$, (d) $Gr_q^* = 3.98$.

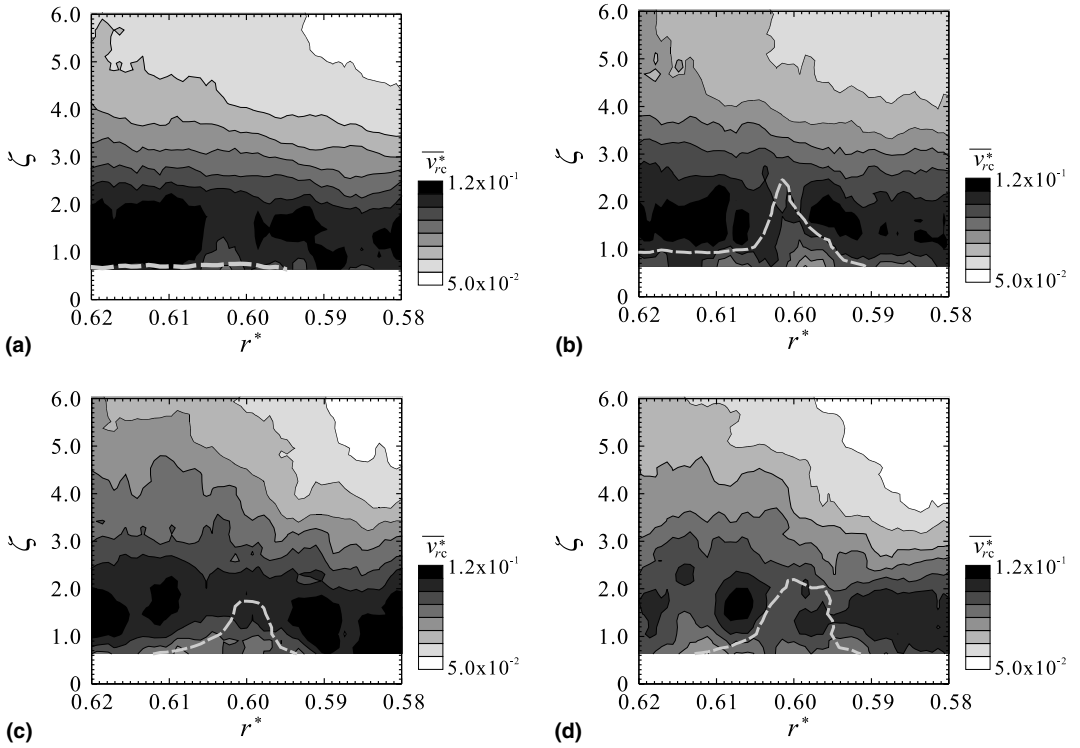

Fig. 10. Distributions of the conditionally averaged radial velocity. (a) $Gr_q^* = 1.79$, (b) $Gr_q^* = 2.76$, (c) $Gr_q^* = 3.13$, (d) $Gr_q^* = 3.98$.

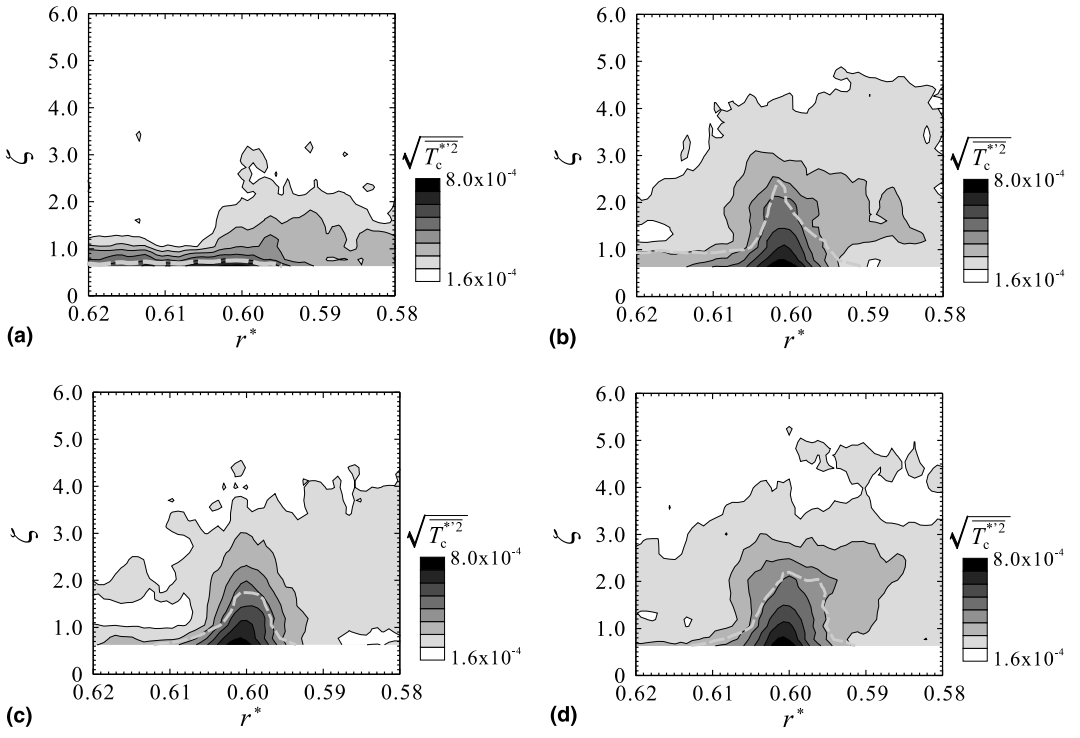

Fig. 11. Distributions of the conditionally averaged RMS value of the temperature fluctuation. (a) $Gr_q^* = 1.79$, (b) $Gr_q^* = 2.76$, (c) $Gr_q^* = 3.13$, (d) $Gr_q^* = 3.98$.

3.2. Frequency of appearance of the vortex

Fig. 5 shows the frequency distributions of the time interval between the successive appearances of the vortex, τ, which is defined in Fig. 4. It is seen from Fig. 5(a) that there are two peaks at around $\tau \approx 1$ s and $\tau \approx 7$ s for $Gr_q^* = 1.79$. However, we could not detect any noticeable difference between two visualized images of the vortices at $\tau \approx 1$ and 7 s. The probability of appearance of the vortices of smaller τ increases and that of larger τ decreases with increasing normalized Grashof number, Gr_q^*.

Fig. 6 shows the dependency of averaged time interval between the successive appearances of vortex, $\overline{\tau}$, on Gr_q^*. As shown in this figure, $\overline{\tau}$ decreases with increasing Gr_q^* and approaches to about 1.7 s at large values of Gr_q^*. In other words, the frequency of the vortex emerging increases with increasing buoyancy effect.

3.3. Instantaneous temperature and velocity distribution

Fig. 7 shows an example of the measured instantaneous temperature and velocity distributions when a vortex passes the measuring point of $r^* = 0.6$ and $\zeta = 0.63$.

As shown in Fig. 7(a), the vortex has a mushroom shape and there exists a high temperature core at the bottom of the vortex. All vortices have such high temperature cores as this one, though there are some variations in shapes of temperature distribution. Another feature of the vortices is noticeable upward flow from the high temperature core to the bulk fluid as shown in Fig. 7(b).

3.4. Distribution of the averaged temperature

Fig. 8 shows the spatial distributions of dimensionless conditionally averaged temperature in the r–z plane obtained by the following equation:

$$\overline{T_c^*}(r^*, \zeta) = \frac{1}{N_c} \sum_{i=1}^{N_c} \frac{T_{ci}(r^*, \zeta) - T_s}{q_w R_d / k}, \tag{5}$$

where $T_{ci}(r^*, \zeta)$ is an instantaneous temperature distribution at the moment that a vortex passes through the measuring point at $r^* = 0.6$ and $\zeta = 0.63$, and N_c is the number of the detected vortices.

Here, we define the vortex shape as the contour line of $\overline{T_c^*} = 8.0 \times 10^{-4}$. From Fig. 8, it is found that the area

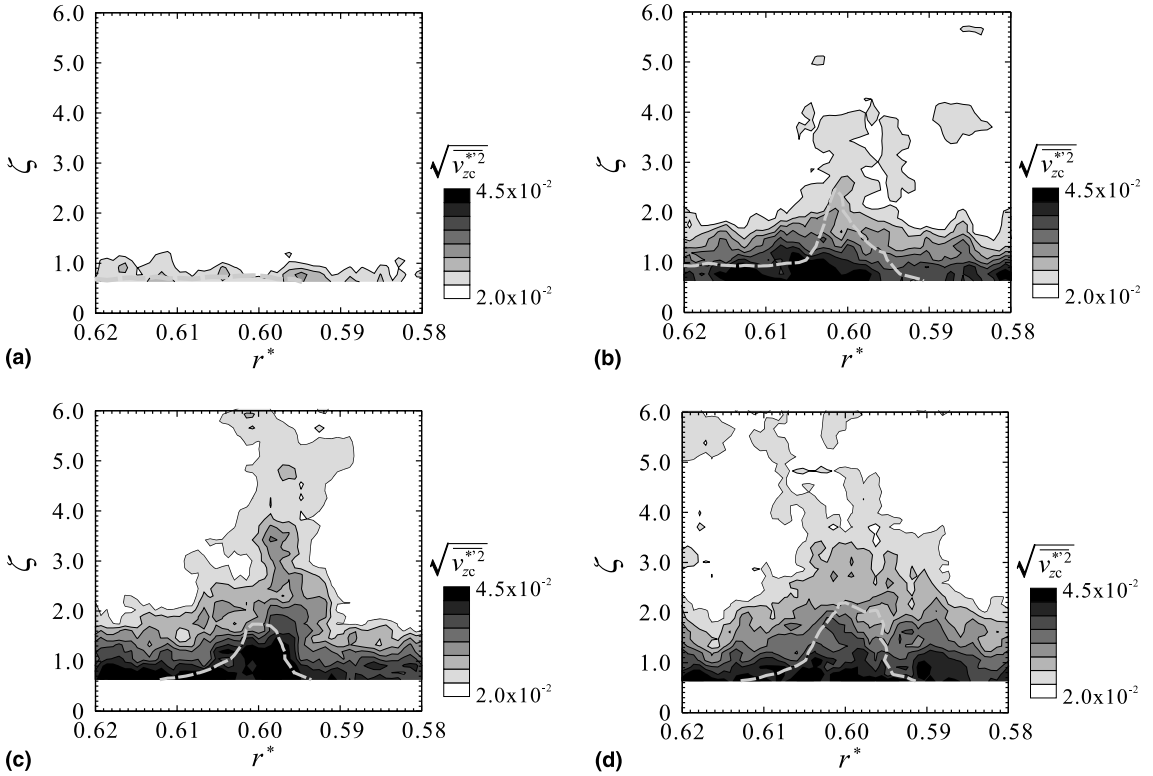

Fig. 12. Distributions of the conditionally averaged RMS value of the vertical velocity fluctuation. (a) $Gr_q^* = 1.79$, (b) $Gr_q^* = 2.76$, (c) $Gr_q^* = 3.13$, (d) $Gr_q^* = 3.98$.

at $\overline{T_c^*}(r^*,\zeta) > 8.0 \times 10^{-4}$ are almost same in size except for $Gr_q^* = 1.79$.

3.5. Distribution of the averaged vertical velocity

Fig. 9 shows the spatial distributions of dimensionless conditionally averaged vertical velocity, $\overline{v_{zc}^*}$, in the r–z plane obtained by the similar method as that of the averaged temperature. The thick curve shows the contour line of $\overline{v_{zc}^*} = 0$ and the broken curve shows the vortex shape defined in 3.4. From Fig. 9, it is found that the value of the upward velocity increases with increasing Gr_q^* especially near the center of the vortex. The height where $\overline{v_{zc}^*}(r^*,\zeta)$ takes its peak is about $\zeta = 1$–2 and the region of higher value of $\overline{v_{zc}^*}$ extends to the right-hand side of the vortex core, the rear side of the vortex which travels in the radial direction from the center to the disc edge, at larger Gr_q^*. The downward flow near the disc surface is caused by the compensating motion for the strong upward motion in the vortex.

3.6. Distribution of the averaged radial velocity

Fig. 10 shows the spatial distributions of dimensionless conditionally averaged radial velocity, $\overline{v_{rc}^*}$, in the r–z plane. The patterns of the contour lines of $\overline{v_{rc}^*}$ are almost same for all Gr_q^*, that is, the values of $\overline{v_{rc}^*}$ are large at the region of $\zeta = 1$–2, although at the vortex core, $r^* = 0.6$, they are somewhat small. This is in accordance with the pattern shown in Fig. 7(b).

3.7. RMS value of the fluctuation

The spatial distributions of the conditionally averaged RMS values of the fluctuations of temperature, vertical and radial velocity components are shown in Figs. 11–13 to evaluate the disturbance when the vortices emerge on the disc.

Fig. 11 shows that the shape of the distributions of $\sqrt{\overline{T_c^{*\prime 2}}}$ are similar to those of $\overline{T_c^*}$, the value of $\sqrt{\overline{T_c^{*\prime 2}}}$ being large at the high temperature core.

Fig. 12 shows that the RMS value of the vertical velocity fluctuation is large near the disc wall regardless of the radial position and is larger in the vortex region than the outside of the vortex at $\zeta > 2$ for large Gr_q^*.

On the other hand, the value of $\sqrt{\overline{v_{rc}^{*\prime 2}}}$ decreases with increasing ζ regardless of the radial position and Gr_q^* as shown in Fig. 13.

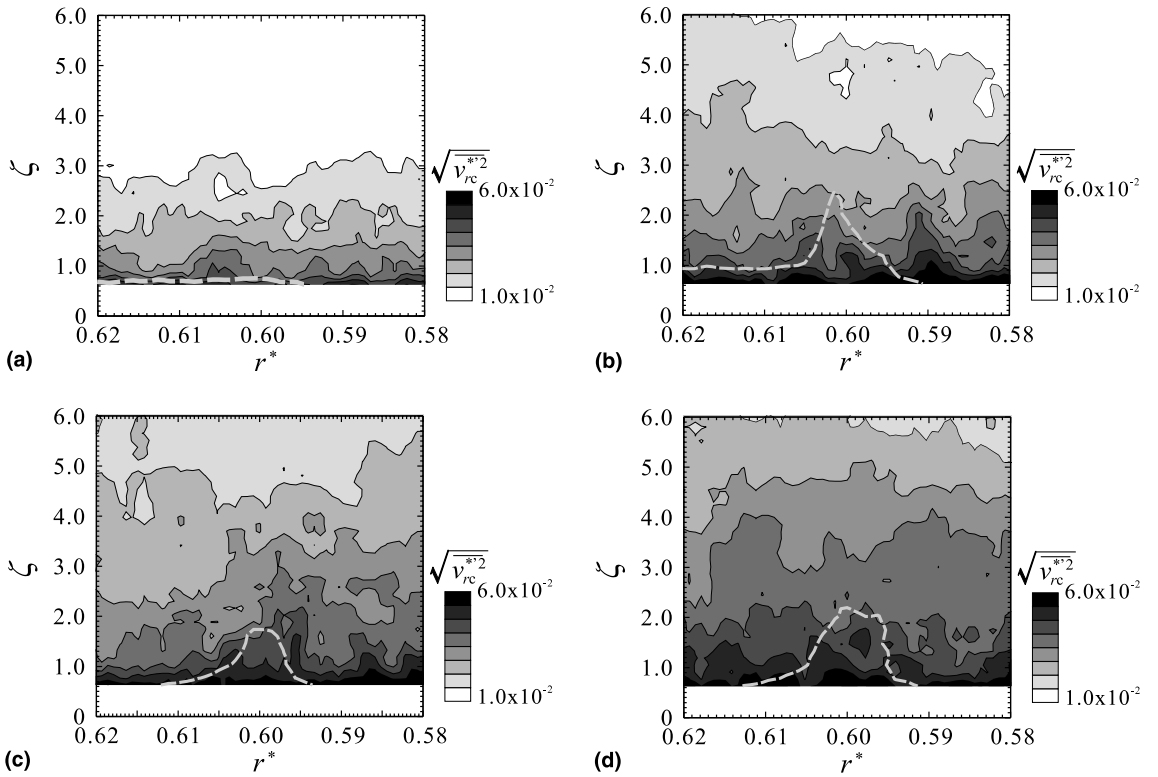

Fig. 13. Distributions of the conditionally averaged RMS value of the radial velocity fluctuation. (a) $Gr_q^* = 1.79$, (b) $Gr_q^* = 2.76$, (c) $Gr_q^* = 3.13$, (d) $Gr_q^* = 3.98$.

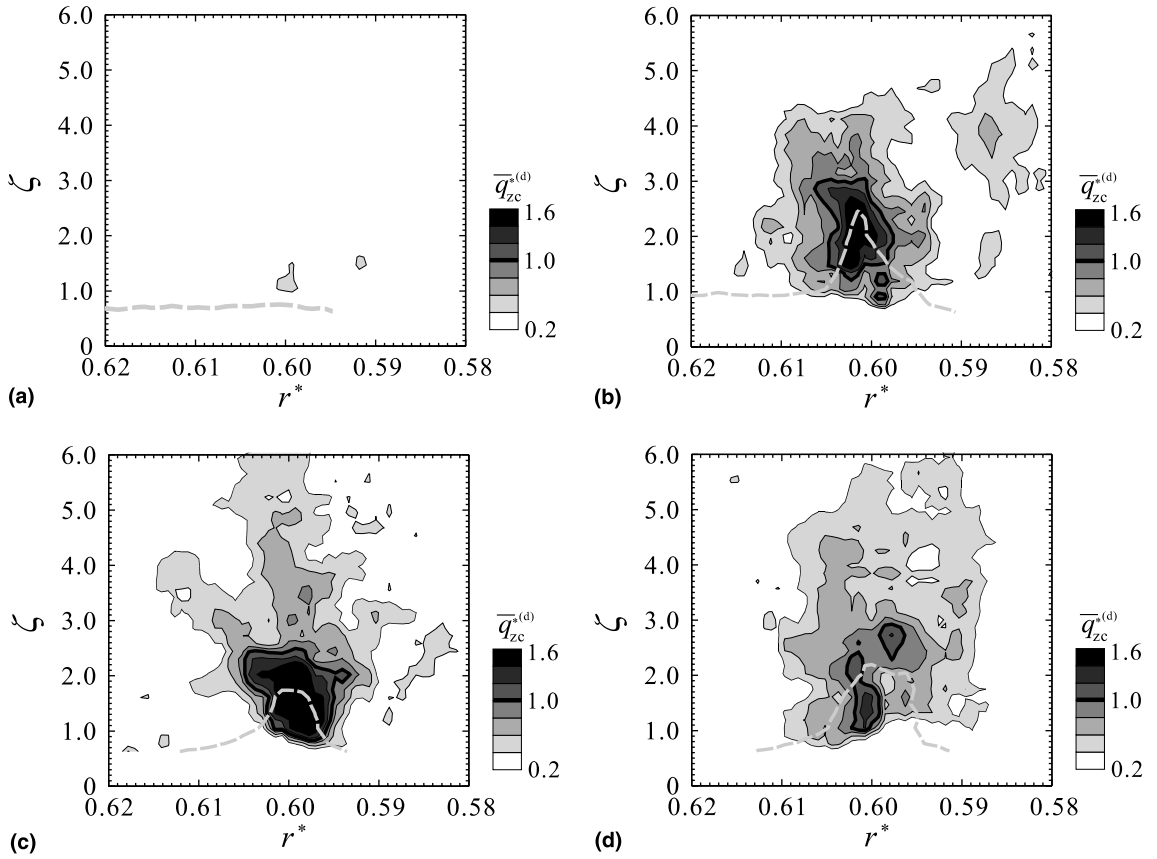

Fig. 14. Distributions of the conditionally averaged vertical heat flux by fluctuation. (a) $Gr_q^* = 1.79$, (b) $Gr_q^* = 2.76$, (c) $Gr_q^* = 3.13$, (d) $Gr_q^* = 3.98$.

3.8. Vertical heat flux by fluctuation

We calculated the vertical heat flux by fluctuation defined by

$$\overline{q_{zc}}^{(d)} = \rho C_p \overline{v'_{zc} T'_c} \tag{6}$$

to estimate the effect of the vortices on the heat transfer.

Fig. 14 shows the spatial distributions of dimensionless conditionally averaged heat flux by fluctuation, $\overline{q^*_{zc}}^{(d)} = \overline{q_{zc}}^{(d)}/q_w$, in the r–z plane. The thick curve shows the contour line of $\overline{q^*_{zc}}^{(d)} = 1.0$. From Fig. 14, it is found that the heat transfer in the upward direction occurs mainly in the vortex and that the height where $\overline{q^*_{zc}}^{(d)}(r^*, \zeta)$ takes its peak is $\zeta = 1$–2 for large Gr_q^*.

4. Conclusions

The results obtained by the present experimental investigation are summarized as follows:

1. The frequency of appearance of the vortex due to buoyancy increases with increasing buoyancy effect and approaches a nearly constant value at large Grashof number.
2. The value of the vertical velocity component is very high in the vortex, whereas that of the radial one is rather small.
3. The RMS values of the temperature and vertical velocity fluctuations are large in the vortex, although that of the radial velocity fluctuation in the vortex is almost same as that of the outside of the vortex.
4. The vertical heat flux by fluctuation in the vortex is larger than that of outside of the vortex, and takes its peak at $\zeta = 1$–2 for large Gr_q^*.

References

[1] H. Schlichting, Boundary Layer Theory, seventh ed., McGraw-Hill, NewYork, 1979, pp. 102–107.
[2] M.R. Malik, S.P. Wilkinson, S.A. Orszag, Instability and transition in rotating flow, AIAA J. 19 (1981) 1131–1138.
[3] S. Balachandar, C.L. Streett, M.R. Malik, Secondary instability in rotating disk flow, J. Fluid Mech. 242 (1992) 323–347.

[4] R.L. Lingwood, An experimental study of absolute instability of the rotating disk boundary layer flow, J. Fluid Mech. 314 (1996) 373–405.
[5] H.S. Littell, J.K. Eaton, Turbulence characteristics of the boundary later on a rotating disk, J. Fluid Mech. 266 (1994) 175–207.
[6] X. Wu, K.D. Squires, Prediction and investigation of the turbulent flow over a rotating disk, J. Fluid Mech. 418 (2000) 231–264.
[7] E.C. Cobb, O.A. Saunders, Heat transfer from a rotating disk, in: Proceedings of the Royal Society of London, Series A, Math. Phys. Sci. 236 (1956) 343–351.
[8] S.T. McComas, J.P. Hartnett, Temperature profiles and heat transfer associated with a single disk rotating in still air, in: U. Grigull, E. Hahne (Eds.), Proceedings of the Fourth International Heat Transfer Conference, Elsevier, Amsterdam, 1970 (FC7.7).
[9] C.O. Popiel, L. Boguslawski, Local heat-transfer coefficients on the rotating disk in still air, Int. J. Heat Mass Transfer 18 (1975) 167–170.
[10] C.J. Elkins, J.K. Eaton, Heat transfer measurements in the boundary layer on a rotating disc, In General Papers in Heat and Mass Transfer, Insulation, and Turbo Machinery, vol. 271, ASME HTD, 1994, pp. 193–200.
[11] S.E. Tadros, F.F. Erian, Heat and momentum transfer in the turbulent boundary layer near a rotating disk, ASME Paper 83-WA/HT-6, 1983.
[12] F. Ogino, Y. Saito, T. Yoshida, K. Masuda, K. Mizuta, Heat transfer and flow characteristics in a rotating disc system, Kagaku Kogaku Ronbunshu 23 (5) (1997) 679–686.
[13] F. Ogino, Y. Saito, T. Yoshida, K. Masuda, K. Mizuta, Heat transfer on a heated rotating disc, in: Proceedings of the 2nd International Symposium on Heat and Mass Transfer, Kansai Branch of the Heat Transfer Society of Japan, Kyoto, 1997, pp. 19–24.
[14] F. Ogino, A. Saito, Y. Saito, Simultaneous measurements of velocity and temperature of the natural convection flow on a heated rotating disc, in: J.S. Lee (Ed.), Proceedings of the Eleventh International Heat Transfer Conference, Taylor & Francis, Philadelphia, PA, 1988, pp. 149–154.
[15] F. Ogino, Y. Saito, H. Matsumoto, Flow near a rotating disc with stagnation flow, Kagaku Kogaku Ronbunshu 23 (5) (1997) 713–719.
[16] J. Sakakibara, K. Hishida, M. Maeda, Measurements of thermally stratified pipe flow using image-processing techniques, Exp. Fluids 16 (1993) 82–96.
[17] C.E. Willert, M. Gharib, Digital particle image velocimetry, Exp. Fluids 10 (1991) 181–193.
[18] Y.A. Hassan, T.K. Blanchat, C.H. Seeley Jr., R.E. Canann, Simultaneous velocity measurements of both components of a two-phase flow using particle image velocimetry, J. Multiphase Flow 18 (3) (1992) 371–395.
[19] G. Wozniak, K. Wozniak, Buoyancy and thermocapillary flow analysis by the combined use of liquid crystals and PIV, Exp. Fluids 17 (1994) 141–146.